New Journal of Physics
The open access journal at the forefront of physics

Deutsche Physikalische Gesellschaft DPG IOP Institute of Physics

PAPER • OPEN ACCESS

The $SrTiO_3/BiFeO_3$ (001) interface: commutativity of energy band discontinuities

To cite this article: R Schafranek *et al* 2013 *New J. Phys.* **15** 053014

New Journal of Physics
The open access journal for physics

The $SrTiO_3/BiFeO_3$ (001) interface: commutativity of energy band discontinuities

R Schafranek[1,2], J D Baniecki[2], M Ishii, Y Kotaka and K Kurihara
Fujitsu Laboratories Ltd, 10-1 Morinosato-Wakamiya, Atsugi 243-0197, Japan
E-mail: rschafranek@surface.tu-darmstadt.de and baniecki@labs.fujitsu.com

New Journal of Physics **15** (2013) 053014 (12pp)
Received 16 November 2012
Published 8 May 2013
Online at http://www.njp.org/
doi:10.1088/1367-2630/15/5/053014

Abstract. The interface formation between the perovskite oxides $SrTiO_3$ and $BiFeO_3$ was studied using *in situ* photoelectron spectroscopy by depositing $BiFeO_3$ on $SrTiO_3$ and vice versa via pulsed laser deposition. For the interfaces characterized, a type II band alignment with a valence band offset of 0.9–1.0 eV and a conduction band offset of 0.5–0.6 eV was observed. Within the margin of error the commutativity was fulfilled for the $SrTiO_3/BiFeO_3$ interface, meaning that the band alignment does not depend on the deposition sequence.

S Online supplementary data available from stacks.iop.org/NJP/15/053014/mmedia

[1] On leave from Darmstadt University of Technology, Institute of Materials Science, Petersenstrasse 23, D-64287 Darmstadt, Germany.
[2] Authors to whom any correspondence should be addressed.

Contents

1. Introduction **2**
2. Experiment **3**
3. Results **4**
3.1. $BiFeO_3$ (BFO) structure 4
3.2. Survey spectra 5
3.3. $SrTiO_3$(STO)/BFO interface formation 6
3.4. STO/BFO interface formation 7
3.5. Band offsets at the STO/BFO and BFO/STO interfaces 8
4. Discussion **10**
5. Conclusion **10**
Acknowledgments **11**
References **11**

1. Introduction

Ferroelectric and paraelectric perovskite oxide thin films have been widely studied based on their various applications in e.g. ferroelectric non-volatile memories [1], infrared imaging detectors [2] and tunable microwave devices [3–5]. While the functionality of these devices depends on the perovskite oxide's ferroelectric or nonlinear dielectric behavior, perovskite oxides are also attracting attention for their application in devices where the unique functionality is due to their transport properties. This includes resistive read access memories or switchable diodes showing a tunable photocurrent under illumination [6, 7]. For instance, the paralectric perovskite material $SrTiO_3$ (STO) shows a resistive switching effect, which is observed when STO is sandwiched between electrodes such as e.g. Pt [6] and which might be explained by the change of electronic transport properties at the STO/electrode interface [8, 9].

The multiferroic $BiFeO_3$ (BFO) has also recently been intensively studied owing to a switchable diode effect depending on the BFO polarization direction [7, 10], although the large leakage currents of BFO [7, 11–13] have limited possible device applications. This issue has been partially addressed by fabrication of STO/BFO bilayer [11] or STO/BFO multilayer systems [14], which lead to a significant reduction in leakage current as compared with pure BFO films, without compromising the ferroelectric properties of BFO. Nevertheless, for the further understanding and optimization of the electronic transport properties across the STO/BFO interfaces, knowledge of the band alignment is crucial, as the discontinuities between the valence and conduction bands at the interface determine the electronic transport properties. However, the knowledge of the band offsets at dielectric perovskite/perovskite interfaces is largely unresolved. Moreover, knowledge of the energetic position of the band edges can also help in understanding the range of dopability of the perovskite oxide semiconductors.

In earlier studies the band alignment of STO with $PbTiO_3$ [15] ($SrZrO_3$ [16]) was characterized to be of type II with a valence band offset $\Delta_{VB} = 1.1$ eV (type I with $\Delta E_{VB} = 0.5$ eV). Furthermore, Qiao *et al* [17] reported the band line-up of STO with $LaAlO_3$ to be of type II with $\Delta E_{VB} = 0.16$ eV. A type I heterojunction is present when the conduction band minimum and valence band maximum (VBM) of the narrower band gap semiconductor lie

within the band gap of the wider band gap semiconductor while in the case of a type II heterojunction the band gaps only partially overlap.

For semiconductors the doping levels (the range of Fermi level position) are limited and the doping levels are governed by the position of the band edges [18]. For STO a range of the Fermi level position of ∼1.5 eV ranging from about 2 till 3.5 eV above the VBM was found, explaining the n-type conductivity of STO up to degenerative doping levels, as the band gap of STO is 3.2 eV. For $PbTiO_3$, which has a comparable band gap of 3.5 eV as STO but a ∼1.1 eV higher lying valence band, a comparable range of Fermi level lies in the center of the band gap, explaining the negligible conductivity of $PbTiO_3$ [15]. Thus, the study of the band offsets at the STO/BFO interfaces may not only allow one to obtain the barriers for electron/hole transport across the STO/BFO interfaces but could also elucidate the range of dopability of BFO.

STO and BFO are oxide semiconductors exhibiting an indirect fundamental band gap of 3.2 [19] and ∼2.8 eV [20, 21], respectively. The top of the valence band of STO is mainly derived from O 2*p* states and the bottom of the conduction band is largely derived from Ti 3*d* states [22]. While in the case of BFO the top of the valence band is as well mainly derived from O 2*p* and the bottom of the conduction band from Fe 4*d* states, A-site cations derived Bi 6*p* states also contribute to the upper valence and lower conduction bands.

In this work, the band alignment between STO and BFO was determined using *in situ* photoelectron spectroscopy during the growth of BFO on STO via pulsed laser deposition and vice versa. This method allows for the simultaneous characterization of the chemical and electronic interface properties which are not accessible from e.g. electronic transport properties or internal photoemission measurements. Furthermore, the band alignment at the STO/BFO and BFO/STO can be decoupled. As the BFO thin films can show large defect concentrations influencing the electronic properties [23], the deposition sequence might influence the electronic interface properties. For the perovskite/perovskite interface studied a type II configuration with a valence band offset $\Delta E_{VB} = 1.0$ eV was found for both interface preparations, showing that the STO/BFO interface behaves commutatively.

2. Experiment

To study the STO/BFO and BFO/STO interface formation, *in situ* photoelectron spectroscopy was performed using an ultra-high vacuum system, combining a photoelectron spectrometer via a transfer chamber with a pulsed laser deposition chamber. The photoelectron spectrometer consists of a custom-made analysis chamber outfitted with a PHOIBOS 100 hemispherical analyzer and a two-dimensional charge-coupled device detector, both from SPECS. A monochromatized Al Kα excitation source was used for x-ray-induced photoelectron spectroscopy (XPS). Spectra were recorded in normal emission. Binding energies are given with respect to the Fermi energy, as calibrated with as-prepared metal films.

To characterize the STO/BFO interface, thin, insulating BFO films were grown on highly conductive (001)-oriented 1 wt% niobium-doped STO (STO:Nb) single crystals to rule out charging effects during XPS measurements. The substrates were first subjected *ex situ* to an annealing step at 1000 °C in an 80% N_2/20% O_2 atmosphere in a quartz tube furnace for 3 h, to obtain a step-terrace surface with mixed SrO / TiO_2 termination [24]. Furthermore, prior to the interface experiments the single crystals were subjected *in situ* to a heat treatment at 600 °C in 200 mTorr oxygen to remove any surface contaminations, as checked for by XPS.

The BFO (nominally undoped STO (I-STO)) thin films were deposited using a q-switched Nd:YAG laser with a pulse rate of 10 Hz and a laser fluence of 1.25 (1.6) J cm^{-2} from a ceramic BFO (nominally undoped single-crystalline STO) target at a target to substrate distance of 5 cm. The substrate temperature was set to 600 °C and an oxygen pressure of 200 (1) mTorr was used, leading to a deposition rate of ∼0.8 (1.8) nm min^{-1}, as deduced from the attenuation of the STO:Nb (BFO) substrate emission during BFO (intrinsic STO) growth via XPS using inelastic mean free paths calculated after [25]. The BFO thin film stoichiometry was checked for by inductively coupled plasma optical emission spectroscopy.

The BFO/STO interface was studied during deposition of intrinsic STO thin films on a ∼10nm thick BFO film prepared on the aforementioned (001)-oriented 1 wt% niobium-doped STO single crystals.

The characterization of the BFO thin film structure was carried out on the ∼13 nm thick BFO film grown on a STO:Nb (001) single crystal during the STO/BFO interface experiment by means of x-ray diffraction using a Philiphs X'Pert Pro thin film diffractometer. In addition, Cs-corrected high angle annular dark field scanning transmission electron microscopy (HAADF-STEM) images of said BFO film grown on STO:Nb were recorded with a JEOL 200 kV JEM-2100F TEM/STEM equipped with a *CEOS* aberration corrector. The Cs of our instrument is estimated by probe tableau calculation to be less than 1 mm.

Furthermore, structural information of the BFO (∼10 nm)/*I*-STO (∼14 nm) layer stack grown on STO:Nb during the BFO/STO interface experiment was recorded using x-ray diffraction.

3. Results

3.1. $BiFeO_3$ (BFO) structure

To confirm the epitaxial BFO (001) growth on STO:Nb (001), x-ray diffraction patterns were recorded in θ–2θ geometry as shown in figure 1(a), where only STO (00l) and BFO (00l) reflections are visible. Furthermore, as shown in the inset in figure 1(a), the BFO film and STO substrate reflections line up in the (101) ϕ-scan. While the STO single-crystal reflection positions are in accordance with the cubic lattice of STO with a lattice parameter of 0.3905 nm, the BFO out-of-plane lattice parameter of ∼0.404 nm is significantly higher than the pseudocubic lattice parameter of 0.3965 nm for rhobohedral BFO, which has been reported before for ∼50 nm thick BFO epitaxial thin films grown on STO (001) [26].

The epitaxial growth of BFO on STO:Nb (001) is supported by the HAADF-STEM cross-sectional image of the STO:Nb (001)/BFO interface presented in figure 1(b). Here no misfit dislocations are visible for the BFO film thickness of ∼13 nm, which is in accordance with the small lattice mismatch between STO and pseudocubic BFO of ∼1.5%. For $BaTiO_3$ deposited on STO which has a larger lattice mismatch of 2.2%, the critical thickness for misfit dislocation formation was reported to be between 10 [27] and 5 nm or less [28]. The absence of misfit dislocations in figure 1(b) allows us to conclude that the BFO films grow coherently strained on the STO:Nb (001) substrate. The biaxial compressive stress state of the BFO thin film grown on the STO leads to the observed extension of the BFO out-of-plane lattice parameter.

Furthermore, the x-ray diffraction pattern recorded in θ–2θ geometry and ϕ-scan of the BFO/I-STO layer stack grown on STO:Nb during the BFO/STO interface experiment are

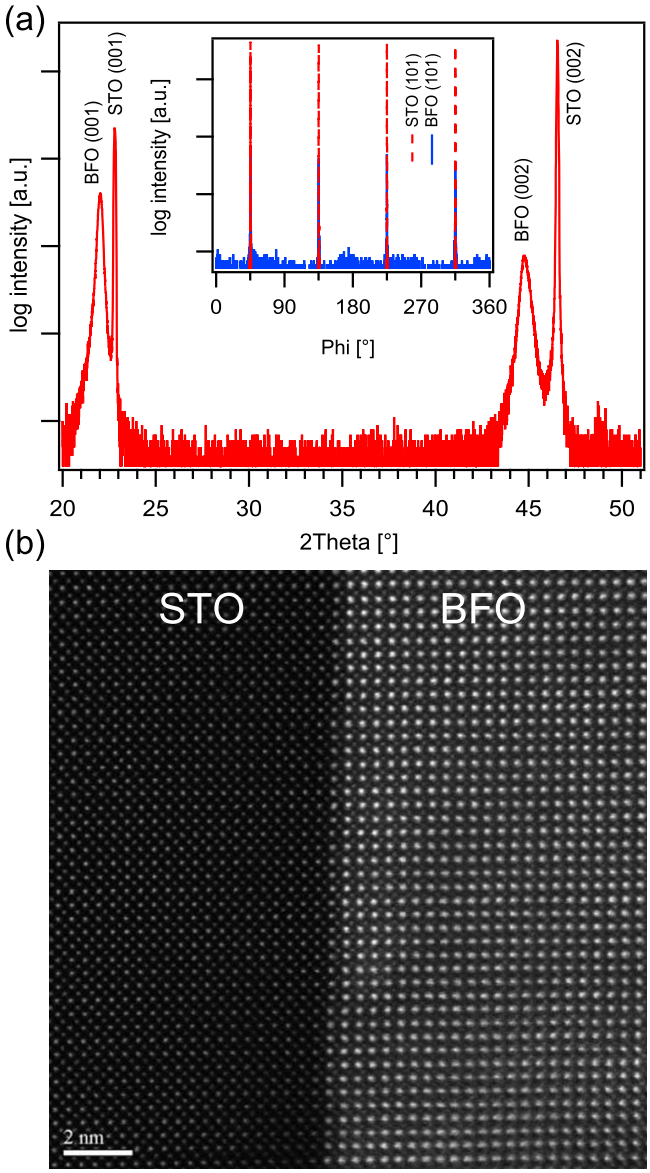

Figure 1. (a) X-ray diffraction pattern and (101) ϕ-scan (inset) of the ∼13 nm thick BFO thin film deposited on a Nb:STO (001) single-crystal substrate. (b) HAADF-STEM cross-sectional image of the interface between STO:Nb (001) and the ∼13 nm thick BFO film.

shown in supplementary figure S1 (available from stacks.iop.org/NJP/15/053014/mmedia). Neither in the diffraction pattern nor in the ϕ-scan additional reflections can be observed indicating epitaxial growth of I-STO on BFO.

3.2. Survey spectra

Figure 2 shows normalized x-ray-induced survey spectra of the STO surface after oxygen cleaning as well as of the ∼13 nm thick BFO thin film deposited during the interface experiment.

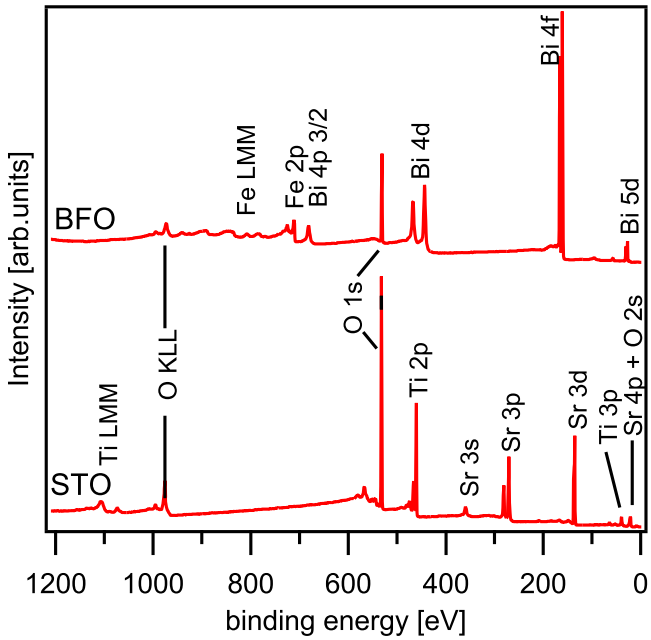

Figure 2. X-ray-induced survey spectra of the STO:Nb substrate and of the ∼13 nm thick BFO thin film deposited on STO:Nb normalized to their maximum intensity.

In the case of STO (BFO) only emissions of the elements Sr, Ti and O (Bi, Fe, O) are visible. No adventious carbon (binding energy ∼285 eV) could be observed, which would lie at slightly smaller binding energies compared with the Sr $3p_{1/2}$ emission of STO.

3.3. $SrTiO_3$(STO)/BFO interface formation

In figure 3, x-ray-induced photoelectron core level spectra of the STO substrate and BFO deposit are presented during the stepwise deposition of BFO on STO:Nb. The intensity of the Sr $3d$ and Ti $2p$ emissions decreases with increasing BFO film thickness until in the case of the ∼13 nm thick BFO film the Sr and Ti substrate emissions are completely attenuated. The intensity of both substrate emissions decreases exponentially with decay constants corresponding to their inelastic mean free paths (∼2.25 nm (Sr $3d$) and ∼1.8 nm (Ti $2p$) (after [25])) indicating layer-by-layer growth of BFO on STO:Nb. In the Ti $2p$ spectra at ∼466 eV the Bi $4d_{3/2}$ emission appears for larger BFO thicknesses with its intensity increasing in parallel with the Bi $4f_{7/2}$ and Fe $2p$ deposit emissions shown in figure 3. The Bi $4f_{7/2}$ and Fe $2p$ emissions are characteristic of Bi^{3+} and Fe^{3+}. The asymmetry of the Fe $2p_{3/2}$ and Fe $2p_{1/2}$ emission at binding energies at ∼710 and 723 eV is due to the multiplet structure of Fe^{3+} while the shake-up satellites at ∼719 and 732 eV are also characteristic of Fe^{3+} [29].

The lineshape of the STO substrate and BFO deposit emissions remains almost constant with increasing BFO deposit thickness. For the Sr $3d$ and Ti $2p$ substrate emissions, only a small increase of the full-width at half-maximum (FWHM) from ∼0.8 to ∼1.0 eV and for the Bi $4f_{7/2}$ emission a decrease of FWHM from ∼1.05 to ∼0.85 eV is observed with increasing BFO thickness. Sr $3d$, Ti $2p$ and Bi $4f_{7/2}$ FWHM and binding energy positions are documented in

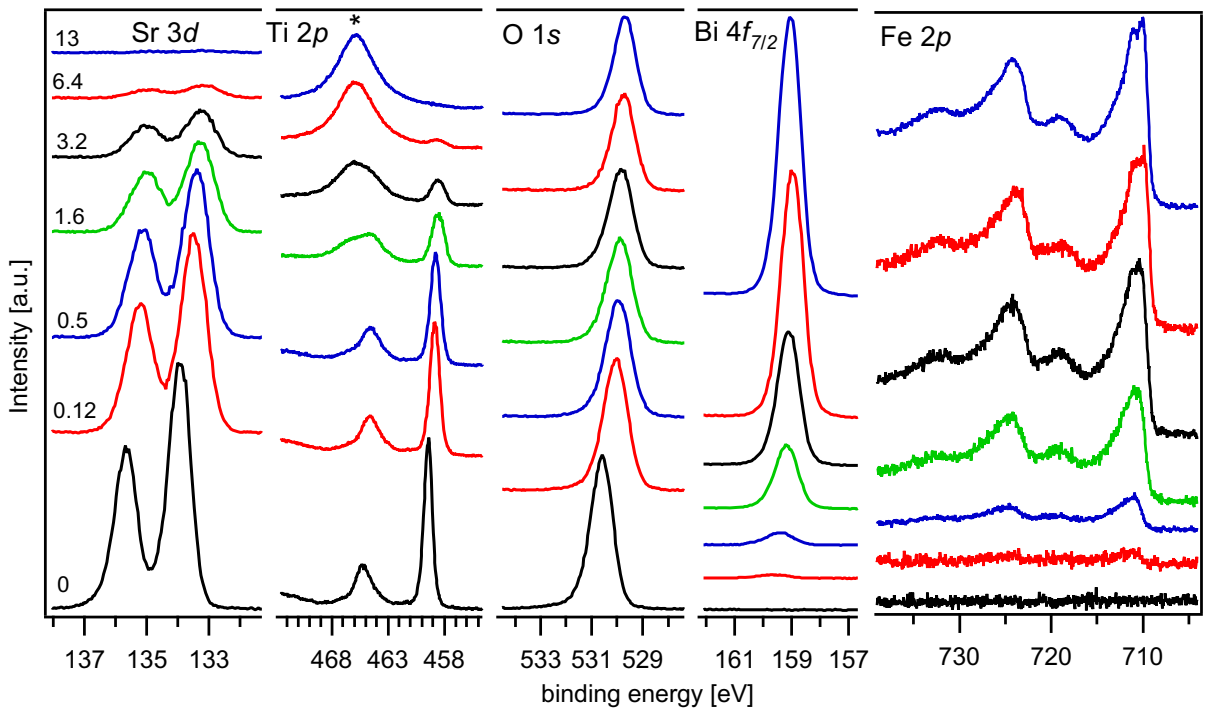

Figure 3. X-ray-induced core level spectra of STO:Nb recorded during the interface formation with BFO. The BFO thickness is given in nm. In the Ti 2*p* spectra the Bi $4d_{3/2}$ emission marked with an asterisk is visible at ∼466 eV for large BFO film coverages.

supplementary table S1 (available from stacks.iop.org/NJP/15/053014/mmedia). In case of the Fe 2*p* emission, showing a more complicated multiplet structure, the FWHM also decreases slightly with increasing BFO thickness. The shake-up satellite in the Fe 2*p* emission at ∼719 and 732 eV, attributed to Fe^{3+}, is visible for BFO film thicknesses of ∼0.5 nm and above. The STO substrate and the BFO film emission lines show a parallel shift toward smaller binding energies. From the almost constant lineshape of the STO and BFO emissions as well as the parallel shift during the interface experiment, an interface reaction between STO and BFO can be ruled out.

3.4. STO/BFO interface formation

The x-ray-induced photoelectron spectra recorded during the stepwise deposition of I-STO on BFO are shown in figure 4. The intensities of the Bi $4f_{7/2}$ and Fe 2*p* emissions decrease until they are fully attenuated for a STO thickness of ∼14 nm. As in the case of the deposition of BFO on STO:Nb the BFO substrate emissions decrease exponentially with decay constants corresponding to their inelastic mean free paths (∼2.2 nm (Bi $4f_{7/2}$) and ∼1.45 nm (Fe 2*p*) (after [25])) indicating also layer-by-layer growth of I-STO on BFO. After a slight shift toward lower binding energies for a STO thickness of ∼0.15 nm the BFO substrate emissions are shifted in parallel toward larger binding energies. The STO emissions as well show a parallel shift toward larger binding energies. As observed for the STO/BFO interface the lineshape of the substrate and deposit emissions shows no strong change with increasing deposit

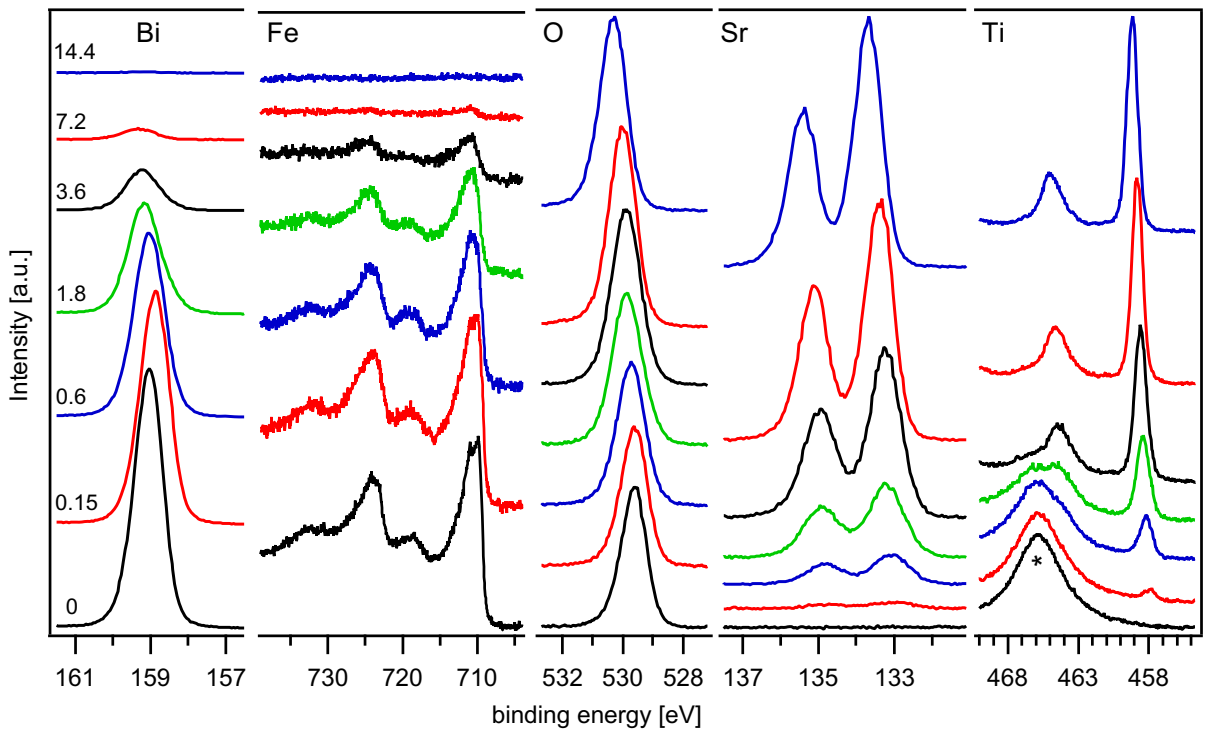

Figure 4. X-ray-induced core level spectra of BFO recorded during the interface formation with intrinsic STO. The I-STO thickness is given in nm. In the Ti $2p$ spectra the Bi $4d_{3/2}$ emission marked with an asterisk is visible at ~466 eV for small STO film coverages.

thickness. The Sr $3d$ and Ti $2p$ deposit emissions show only a small decrease of FWHM from ~1.0 to ~0.8 eV and the FWHM of the Bi $4f_{7/2}$ substrate emission increases from ~0.8 to ~1.0 eV with increasing STO deposit thickness. Sr $3d$, Ti $2p$ and Bi $4f_{7/2}$ FWHM and binding energy positions are documented in supplementary table S2 (available from stacks.iop.org/NJP/15/053014/mmedia). The FWHM of the Fe $2p$ emission increases slightly with increasing STO thickness. The shake-up satellite in the Fe $2p$ emission at ~719 and 732 eV is visible for STO film thicknesses of ~3.6 nm and below. From the almost constant lineshape and the parallel shift of the substrate and film emission lines, an interface reaction can be excluded as well as for the STO/BFO interface.

3.5. Band offsets at the STO/BFO and BFO/STO interfaces

For the determination of the band alignment between STO and BFO, the binding energy positions of the Sr $3d_{5/2}$ and Bi $4f_{7/2}$ core level lines are plotted in figure 5 as a function of the deposit thickness. Core level to VBM binding energy differences were subtracted for a better comparison. The Ti and Fe binding energy positions are excluded due to the proximity of the Ti $2p$ and the Bi $4d_{3/2}$ emission lines as well as the multiplet splitting-induced breadth of the Fe $2p_{3/2}$ emission, which could distort the binding energy position determination.

The binding energy evolution in the case of the BFO deposition on STO:Nb is shown in figure 5(a). The Sr $3d_{5/2}$ and Bi $4f_{7/2}$ binding energy positions are referenced to the XP VBM of

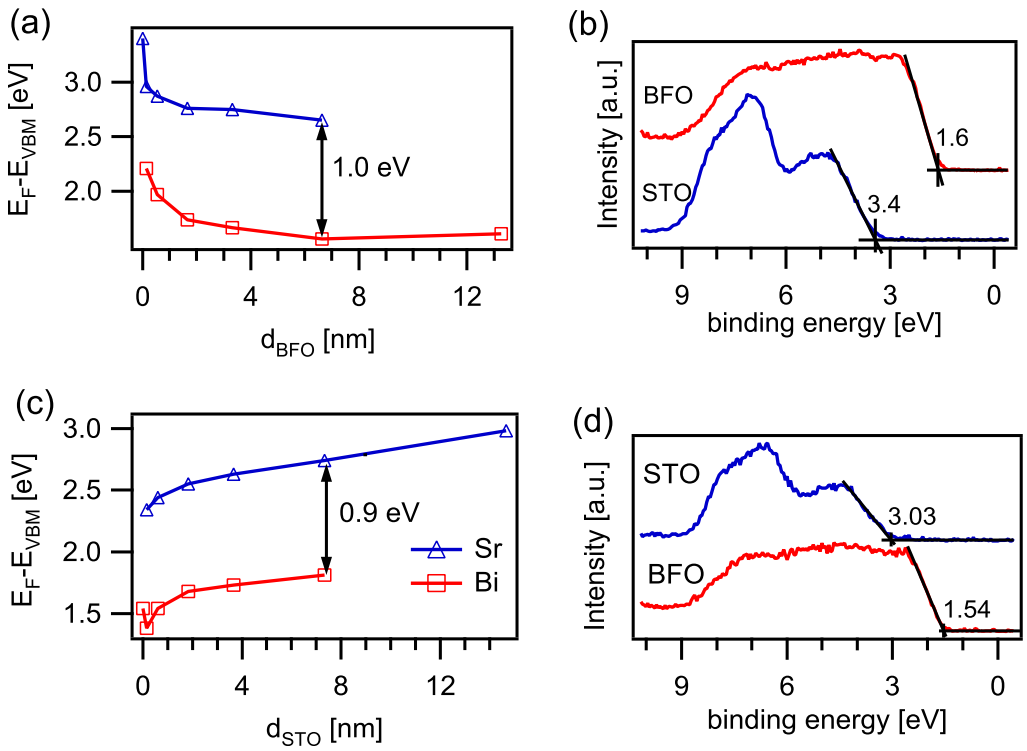

Figure 5. (a) Evolution of the Sr $3d_{5/2}$ and Bi $4f_{7/2}$ core level lines with increasing BFO thickness during the deposition of BFO on STO:Nb and (b) valence band spectra of the STO:Nb substrate and ∼13 nm thick BFO thin film. (c) Evolution of the Sr $3d_{5/2}$ and Bi $4f_{7/2}$ core level lines with increasing I-STO thin film thickness deposited on BFO and (d) valence band spectra of the uncovered BFO substrate and the ∼14 nm thick I-STO thin film deposited on BFO. Core level to valence band maximum binding energy differences were subtracted for better comparison.

the uncovered STO:Nb substrate and the ∼13 nm thick BFO film for a better comparison (see also [15]).

The XP valence band spectra are shown in figure 5(b) with the VBM being derived from the leading edge of the respective valence band. The valence band maxima positions are 3.40± 0.05 and 1.60± 0.05 eV for STO and BFO, respectively. The binding energy positions of the Sr $3d$ and the Bi $4f$ emissions (representing the VBM of STO and BFO, respectively) are shifted toward lower binding energies. The shift of the Bi $4f$ emission is not in parallel with the Sr $3d$ emission as would be expected for a shift of the surface Fermi energy position and could be explained by an evolution of the electronic structure of BFO with film thickness. Therefore, the valence band offset between STO and BFO can be most reliably deduced for the thickest BFO thickness at which both Sr $3d$ and Bi $4f$ emissions can be observed, namely for a BFO film thickness of ∼6 nm. This leads to a valence band offset of 1.0± 0.1 eV with a deeper lying STO valence band. Taking the band gaps of 3.2 eV for STO [19] and 2.8 eV for BFO [20] into account this leads to a conduction band offset of 0.6± 0.1 eV.

The evolution of the Sr $3d_{5/2}$ and Bi $4f_{7/2}$ emissions in the case of the deposition of STO on BFO is shown in figure 5(c). Here the binding energies are referenced to the valence band maxima of the uncovered BFO thin film and the ∼14 nm thick I-STO thin film deposited on

BFO during the interface experiment, respectively. The XP valence band spectra are shown in figure 5(d). The valence band maxima positions are 1.54± 0.05 and 3.03± 0.05 eV for BFO and STO, respectively. Here the Sr 3*d* and Bi 4*f* emissions shift almost parallel toward higher binding energies and for a STO film thickness of ∼7 nm a valence band offset of 0.9± 0.1 eV with a deeper lying STO valence band can be derived, being equal to a conduction band offset of 0.5± 0.1 eV.

4. Discussion

The knowledge of the band alignments at (perovskite) oxide heterostructures is of utmost importance for the understanding and optimization of (perovskite) oxide-based devices, as the electronic transport properties are governed by the band line-ups. However, the understanding of the band alignments at (perovskite) oxide interfaces is still limited. For II–VI semiconductors, small valence band offsets have been predicted for a given anion [30] (the so-called *common anion rule*). Therefore, negligible valence band offsets might be expected for (perovskite) oxide interfaces.

We have recently shown that, for instance, in the case of the $PbTiO_3$/STO interface the *common anion rule* is not fulfilled, as a type II interface with a valence band offset of 1.1± 0.1 eV was observed. In the case of the $PbTiO_3$/STO interface, the large upward shift of the $PbTiO_3$ valence band with respect to STO was attributed to the admixture of Pb 6*s* states with the O 2*p*-derived valence band [15]. In the case of BFO also states of the A-cation, namely Bi 6*p* states, are contributing to the band edges and might be responsible for the reported upward shift of the BFO band edges.

Furthermore, the ∼0.9–1.0 eV higher lying valence band with respect to STO can explain the electronic transport properties of BFO, as the range of Fermi level position is limited due to self-compensation and the doping levels are governed by the position of the band edges [18]. For STO a range of Fermi level position of ∼1.5 eV ranging from about 2 eV till 3.5 eV above the VBM was found, explaining the n-type conductivity of STO up to degenerative doping levels, as the band gap of STO is 3.2 eV. For $PbTiO_3$ with its ∼1.1 eV higher lying valence band a comparable range of Fermi level lies in the center of the band gap, explaining the negligible conductivity of $PbTiO_3$ [15]. In the case of BFO with a VBM ∼0.9–1.0 eV above the STO VBM and its small band gap of ∼2.8 eV the range of Fermi level position appears to lie closer to the conduction band, in contrast to $PbTiO_3$ with a band gap of 3.4 eV [1]. This might explain the large leakage currents found in BFO thin films [7, 11–13] as compared with e.g. $PbTiO_3$.

Finally, from our experiments it follows that in the case of the STO/BFO and BFO/STO interfaces the band offsets are within the experimental uncertainty commutative. This means that the band alignments do not depend on the deposition sequence, fortifying that the band offsets between STO and BFO are governed by the bulk properties of the two perovskite materials as opposed to the local interface environment [31]. To our knowledge this has been shown for the first time for an interface between two (perovskite) oxide materials.

5. Conclusion

The interface formation between STO and BFO has been studied using *in situ* photoelectron spectroscopy. Thin BFO thin films were grown using pulsed laser deposition on (001)-oriented

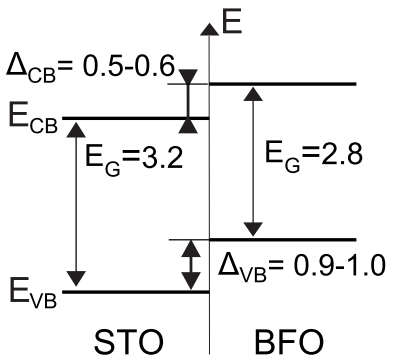

Figure 6. Schematic representation of the band line-up observed at the BFO/STO interface. All energies are given in eV.

Nb-doped STO single-crystal surfaces. The epitaxial growth of BFO (001) on STO (001) was confirmed via XRD and HAADF-STEM. To verify whether the STO/BFO interface is commutative thin undoped STO thin films were grown by pulsed laser deposition on a ∼10 nm thick BFO thin film deposited on a (001)-oriented Nb-doped STO singly crystal. The STO/BFO interface is commutative within the margin of error and a type II band alignment with a valence band offset of 0.9–1.0 eV and a conduction band offset of 0.5–0.6 eV was observed, as shown in the schematic representation in figure 6. In this study the commutativity of the band line-up between (perovskite) oxides has been shown for the first time.

Acknowledgments

Financial support was provided by the National Institute of Information and Communications Technology (NICT) of Japan through the Japan Trust Program and through the Fujitsu Visiting Research Scientist Program.

References

[1] Scott J F 2000 *Ferroelectric Memories* (Heidelberg: Springer)
[2] Whatmore R W 1986 Pyroelectric devices and materials *Rep. Prog. Phys.* **49** 1335–86
[3] Tagantsev A K, Sherman V O, Astafiev K F, Venkatesh J and Setter N 2003 Ferroelectric materials for microwave tunable applications *J. Electroceram.* **11** 5–66
[4] Gevorgian S 2009 Agile microwave devices *IEEE Microw. Mag.* **10** 93–8
[5] Schafranek R, Giere A, Balogh A G, Enz T, Zheng Y, Scheele P, Jakoby R and Klein A 2009 Influence of sputter deposition parameters on the properties of tunable barium strontium titanate thin films for microwave applications *J. Eur. Ceram. Soc.* **29** 1433–42
[6] Sawa A 2008 Resistive switching in transition metal oxides *Mater. Today* **11** 28–36
[7] Choi T, Lee S, Choi Y J, Kiryukhin V and Cheong S W 2009 Switchable ferroelectric diode and photovoltaic effect in $BiFeO_3$ *Science* **324** 63–6
[8] Kim H, Park C, Lee S and Kim D-W 2009 Inhomogeneous barrier and hysteretic transport properties of Pt/$SrTiO_3$ junctions *J. Phys. D: Appl. Phys.* **42** 055306
[9] Lee E, Gwon M, Kim D-W and Kim H 2011 Resistance state-dependent barrier inhomogeneity and transport mechanisms in resistive-switching Pt/$SrTiO_3$ junctions *Appl. Phys. Lett.* **98** 132905

[10] Lee D, Baek S H, Kim T H, Yoon J G, Folkman C M, Eom C B and Noh T W 2011 Polarity control of carrier injection at ferroelectric/metal interfaces for electrically switchable diode and photovoltaic effects *Phys. Rev.* B **84** 125305

[11] Bose S and Krupanidhi S B 2007 Improved ferroelectric and leakage properties in symmetric $BiFeO_3/SrTiO_3$ superlattice *Appl. Phys. Lett.* **90** 212902

[12] Lee W-M, Sung J H, Chu K, Moya X, Lee D, Kim C-J, Mathur N D, Cheong S-W, Yang C-H and Jo M-H 2012 Spatially resolved photodetection in leaky ferroelectric $BiFeO_3$ *Adv. Mater.* **24** OP49–53

[13] Shuai Y, Zhou S, Streit S, Reuther H, Burger D, Slesazeck S, Mikolajick T, Helm M and Schmidt H 2011 Reduced leakage current in $BiFeO_3$ thin films with rectifying contacts *Appl. Phys. Lett.* **98** 232901

[14] Ranjith R, Kundys B and Prellier W 2007 Periodicity dependence of the ferroelectric properties in $BiFeO_3/SrTiO_3$ multiferroic superlattices *Appl. Phys. Lett.* **91** 222904

[15] Schafranek R, Li S, Chen F, Wu W and Klein A 2011 $PbTiO_3/SrTiO_3$ interface: energy band alignment and its relation to the limits of Fermi level variation *Phys. Rev.* B **84** 045317

[16] Schafranek R, Baniecki J D, Ishii M, Kotaka Y, Yamanka K and Kurihara K 2012 Band offsets at the epitaxial $SrTiO_3/SrZrO_3$ (001) heterojunction *J. Phys. D: Appl. Phys.* **45** 055303

[17] Qiao L, Droubay T C, Shutthanandan V, Zhu Z, Sushko P V and Chambers S A 2010 Thermodynamic instability at the stoichiometric $LaAlO_3/SrTiO_3$ (001) interface *J. Phys.: Condens. Matter* **22** 312201

[18] Walukiewicz W 2001 Intrinsic limitations to the doping of wide-gap semiconductors *Physica* B **302–303** 123–34

[19] Cardona M 1965 Optical properties and band structure of $SrTiO_3$ and $BaTiO_3$ *Phys. Rev.* **140** A651

[20] Clark S J and Robertson J 2007 Band gap and Schottky barrier heights of multiferroic $BiFeO_3$ *Appl. Phys. Lett.* **90** 132903

[21] Himcinschi C, Vrejoiu I, Friedrich M, Nikulina E, Ding L, Cobet C, Esser N, Alexe M, Rafaja D and Zahn D R T 2010 Substrate influence on the optical and structural properties of pulsed laser deposited $BiFeO_3$ epitaxial films *J. Appl. Phys.* **107** 123524

[22] Piskunov S, Heifets E, Eglitis R I and Borstel G 2004 Bulk properties and electronic structure of $SrTiO_3$, $BaTiO_3$, $PbTiO_3$ perovskites: an *ab initio* HF/DFT study *Comput. Mater. Sci.* **29** 165–78

[23] Zhang J, Rutkowski M, Martin L W, Conry T, Ramesh R, Ihlefeld J F, Melville A, Schlom D G and Brillson L J 2009 Surface, bulk and interface electronic states of epitaxial $BiFeO_3$ films *J. Vac. Sci. Technol.* B **27** 2012–4

[24] Baniecki J D, Ishii M, Kurihara K, Yamanaka K, Yano T, Shinozaki K, Imada T and Kobayashi Y 2009 Chemisorption of water and carbon dioxide on nanostructured $BaTiO_3$-$SrTiO_3$ (001) surfaces *J. Appl. Phys.* **106** 054109

[25] Cumpson P K and Seah M P 1997 Elastic scattering corrections in AES and XPS: II. Estimating attenuation lengths and conditions required for their valid use in overlayer/substrate experiments *Surf. Interface Anal.* **25** 430–446

[26] Shelke V, Harshan V N, Kotru S and Gupta A 2009 Effect of kinetic growth parameters on leakage current and ferroelectric behavior of $BiFeO_3$ thin films *J. Appl. Phys.* **106** 104114

[27] Lee G H, Shin B C and Kim I S 2001 Critical thickness of $BaTiO_3$ film on $SrTiO_3$ (001) evaluated by reflection high-energy electron diffraction *Mater. Lett.* **50** 134–7

[28] Suzuki T, Nishi Y and Fujimoto M 1999 Analysis of misfit relaxation in heteroepitaxial $BaTiO_3$ thin films *Phil. Mag.* A **79** 2461–83

[29] Fujii T, de Groot F M F, Sawatzky G A, Voogt F C, Hibma T and Okada K 1999 *In situ* XPS analysis of various iron oxide films grown by NO_2-assisted molecular-beam epitaxy *Phys. Rev.* B **59** 3195–202

[30] Zhang S B, Wei S-H and Zunger A 1998 A phenomenological model for systemization and prediction of doping limits in II–VI and I–III–VI_2 compounds *J. Appl. Phys.* **83** 3192

[31] Franciosi A and Van de Walle C G 1996 Heterojunction band offset engineering *Surf. Sci. Rep.* **25** 1–140